

Enhanced Electron Collection and Light Harvesting of $\text{CH}_3\text{NH}_3\text{PbI}_3$ Perovskite Solar Cells Using Nanopatterned Substrates

Chia-Hua Chan,* Chang-Rong Lin, Mai-Chih Liu, Kun-Mu Lee, Zhong-Jia Ji, and Bo-Chiau Huang

In this study, a $\text{CH}_3\text{NH}_3\text{PbI}_3$ -based perovskite solar cell (PSC) with high power conversion efficiency (PCE) has achieved by incorporating a nanopatterned fluorine-doped tin oxide (FTO) substrate (NPFS). This NPFS-PSC is prepared with different structural depths (100, 150, and 200 nm) using both self-assembly and sphere lithography techniques. As determined through the optical and electrical analysis of different PSC devices, the NPFS-PSCs not only display the enhanced light absorption (due to the 2D diffraction grating) but also improve the electron collection efficiency by increasing the FTO/electron transport layer (ETL) and ETL/perovskite effective interface area. Compared to a planar PSC, the photocurrent density of the 200 nm etched NPFS-PSC is enhanced from 19.27 to 23.81 mA cm^{-2} leading to an increase in the PCE from 14.21% to 17.85%. These results indicate that introducing the NPFS into the TiO_2 -based PSC can improve both light absorption ability and electron extraction and, therefore, represents a novel, promising, high-performance photovoltaic device.

PSCs have been receiving this tremendous attention due to their high conversion efficiency, broad light absorption spectrum range, low nonradiative carrier recombination rates, high carrier mobility, long charge-carrier diffusion length, compatible for flexible substrates, and low-cost solution-processing. These features, in addition to low material and production costs, have allowed PSCs to realize the potential of PV. For the $\text{CH}_3\text{NH}_3\text{PbI}_3$ (MAPbI₃)-based PSC specifically, the power conversion efficiency (PCE) has improved considerably up to 22.1% from 3.8% when it was first introduced in 2009.^[1–4] In general, PSCs are fabricated by either thermal evaporation or solution processing (one-step deposition, two-step deposition, and solution to solution extraction).^[5–9] Structurally, a simple PSC consists of several functional

1. Introduction

Organic–inorganic halide perovskite solar cells (PSCs) are photovoltaic (PV) devices whose unique features have rendered them the fastest-advancing solar cell technology to date.

layers that include a transparent conductive oxide (TCO) cathode, an electron transport layer (ETL), a light-harvesting active layer (absorber layer), a hole transport layer (HTL), and a metal anode. After absorbing the incident photons, carriers are generated in the light-harvesting active layer and then collected by the electrode (anode or cathode) in the transport layer (HTL or ETL). For this type of sandwiched optoelectronic device, the electrical properties (carrier recombination, carrier collection efficiency, and defect density) and the optical properties (Fresnel loss and light absorption length) are the critical components that enable its high-performance. Therefore, it is necessary to precisely manipulate each functional layer to fully actualize the potential of PSCs.

Recently, many studies have proposed novel approaches toward obtaining higher efficiency PSCs, including optimizing the fabrication process, improving the quality of the perovskite film toward increasing carrier mobility and lifetimes, engineering the interface toward matching the energy-level in the device, introducing new materials and developing new scaffold architecture toward enhancing carrier collection efficiency, and more.^[10–16] In terms of ETL development, some publications describe replacing the titanium dioxide (TiO_2) with new materials (Al_2O_3 , ZnO , and TiO_2 -graphene) as the ETL.^[17–22] However, the aforementioned strategies mainly focus on the electrical properties of PSCs, e.g., reducing carrier recombination in the TiO_2 /perovskite layer or providing a more efficient

Prof. C.-H. Chan, Dr. C.-R. Lin, Dr. M.-C. Liu, Z.-J. Ji, B.-C. Huang
Graduate Institute of Energy Engineering
National Central University
No. 300, Zhongda Rd., Zhongli Dist.
Taoyuan City 32001, Taiwan (R.O.C)
E-mail: chiahuac@ncu.edu.tw

Prof. C.-H. Chan
Research Center of New Generation Light Driven Photovoltaic Module
National Central University
No. 300, Zhongda Rd., Zhongli Dist.
Taoyuan City 32001, Taiwan (R.O.C)

Prof. K.-M. Lee
Department of Chemical and Materials Engineering
Chang Gung University
No.259, Wenhua 1st Rd., Guishan Dist.
Taoyuan City 33302, Taiwan (R.O.C.)

Prof. K.-M. Lee
Division of Neonatology
Department of Pediatrics
Chang Gung Memorial Hospital
No.5, Fuxing St., Guishan Dist.
Taoyuan City 33305, Taiwan (R.O.C.)

DOI: 10.1002/admi.201801118

pathway for the carriers to travel from the perovskite absorber layer to the electrode. However, light management also plays an important role in improving the PCE of a PSC by increasing photon absorption from the light source. Toward this end, some researchers have introduced nano/microstructures at the glass/air interface (e.g., nanoimprinting lithography, nano/microroughness); these structures reduce the Fresnel reflection loss, thereby increasing the incident photons and resulting photocurrent.^[23–25] Furthermore, some papers also describe constructing nano/microstructures at the fluorine-doped tin oxide (FTO)/TiO₂ interface that increase the absorption length for the incident light due to the diffraction effect.^[26–28]

MAPbI₃ has a high intrinsic absorption coefficient. However, the thickness of the perovskite film is inextricably linked to the thickness of the TiO₂ mesoporous layer (TiO₂-ml), and the optimum perovskite layer thickness is about 300 nm.^[29–32] With thicker TiO₂ film comes a thicker perovskite layer, which confers more defect density and more carrier recombination at the TiO₂/perovskite interface. Decreasing the thickness of the TiO₂ film can improve the PSC's electrical properties but it also reduces the light-harvesting efficiency. Therefore, research efforts have been dedicated to fabricating nano/micropatterned TiO₂-ml as an alternative ETL that can absorb more photons while maintaining low carrier recombination rates.^[33–35] In essence, a finely tuned balance between the optical and electrical properties of a PSC is required to maximize its efficiency.

In our previous studies, we provided a rapid, straightforward method for creating periodic structures on appropriate substrates by incorporating the self-assembling method and the sphere lithography technique applied in GaN-based light-emitting diode, silicon-based solar cells, and organic light-emitting diode.^[36–39] In this study, we used this technique to fabricate a nanopatterned FTO substrate (NPFS) with a 500 nm structural period. We then applied this NPFS to a MAPbI₃-based PSC to

optimize both its optical and electrical properties with the aim of generating an even higher efficiency PSC.

2. Results and Discussion

In this study, a single-layer array was obtained by depositing the SiO₂ spheres onto the surface of a photoresist-coated FTO glass substrate using the self-assembly method. **Figure 1** delineates the NPFS fabrication process. As shown in **Figure 1**, the sphere arrays are similar to ball lens arrays, which can focus incident light and enable the mask-free process for fabricating the hexagonal nanopatterned photoresist on the FTO substrates.^[36]

To observe the morphology of the different etched FTO, **Figure 2** contains scanning electron microscope (SEM) images of the etched FTO with the individual structural depths of 100, 150, and 200 nm. As shown in **Figure 2**, the structural period of each sample was 500 nm, corresponding to the diameter of the deposited SiO₂ spheres; these nanostructures were arranged in a hexagonal pattern of truncated cones due to the 2D hexagonal packing of the SiO₂ monolayer. Being bombarded with ions is damaging to the FTO surface and causes the resistance of FTO films to increase. **Table 1** lists the sheet resistance of the FTO glass with and without inductively coupled plasma (ICP) dry etching. From these data, we found that the sheet resistance was proportional to the etching depth and the deepest etching was only 200 nm, which was associated with the etching selection ratio between the photoresist and the FTO as well as the focal length of the deposited spheres.

For the purpose of this investigation, three structural depths (100, 150, and 200 nm) for the NPFSs (NPFS-100, NPFS-150, and NPFS-200) were selected by modulating the etching period during the ICP dry etching process. **Figure 3a** contains SEM images (cross-sectional view and top view, inset of **Figure 3a**) of

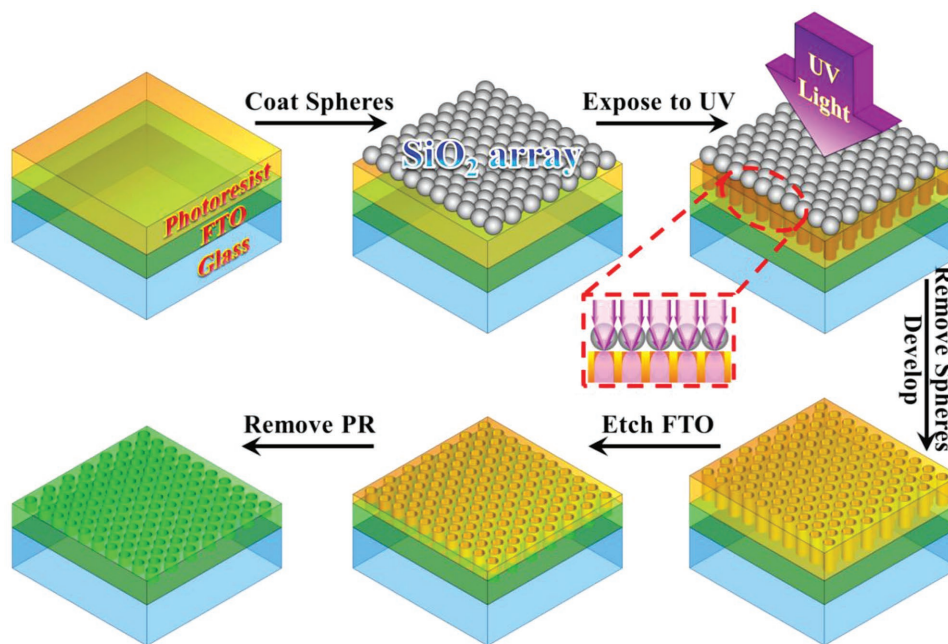


Figure 1. Schematic flow chart of NPFS fabrication.

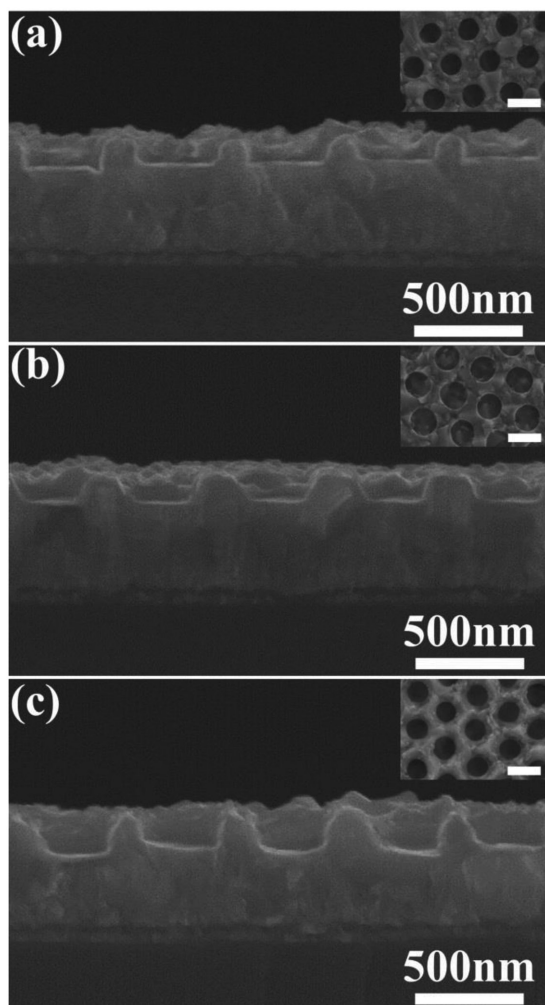


Figure 2. SEM imaging of etched FTO. Side view and top view (inset) of etched FTO with the structural depth of a) 100 nm, b) 150 nm, and c) 200 nm (scale bar: 500 nm), respectively.

a SiO₂ sphere monolayer array (500 nm approximate diameter) deposited onto an FTO glass substrate. This imaging revealed the sphere's highly ordered arrangement with hexagonal packing in two dimensions. Figure 3b shows a cross-sectional view and a top view (inset of Figure 3b) of the nanopatterned photoresist layer on the FTO substrate with a structural period of 500 nm. As shown in Figure 3b, the structural period was related to the diameter of the deposited spheres and the hexagonal arrangement of the nanopatterned photoresist structure corresponded to the hexagonal close-packing of the spheres deposited onto the photoresist layer. Figure 3c contains a

Table 1. Sheet resistance of etched FTO.

Etching depth [nm]	Sheet resistance [$\Omega \square^{-1}$]
w/o	7.00 ± 0.05
100	7.45 ± 0.07
150	8.09 ± 0.03
200	10.12 ± 0.15

cross-sectional and a top view (inset of Figure 3c) image of the NPFS-200 with a vertical etching depth of 200 nm with the same arrangement as in Figure 3b. Figure 3d shows a cross-sectional and a top view (inset of Figure 3d) of the NPFS-200 after (TiO₂ compact layer) TiO₂-cl/TiO₂-ml deposition. Because the TiO₂-ml was deposited onto the NPFS-200, the upper surface of the TiO₂-ml is similar morphologically to the NPFS-200. The film thickness of the TiO₂-ml varies periodically, aligning with the upper surface of the patterned FTO. Figure 3e shows a focused ion beam-assisted cross-sectional SEM image of the NPFS-PSC with a 500 nm structural period and 200 nm etching depth (NPFS-200-PSC). As shown in Figure 3e, the MAPbI₃ active layer was uniformly deposited onto the TiO₂ film with a thickness ranging from 220 to 320 nm and the TiO₂/MAPbI₃ interface exhibited morphology similar to the FTO/TiO₂ interface. Compared to the planar FTO substrate, the NPFS-200 emitted iridescent colors when imaged due to the strong light scattering ability conferred by the nanostructures of the patterned FTO substrate (Figure 3f).

Figure 4 contains the forward scanned (solid line, filled symbols) and reverse scanned (dashed line, open symbols) photocurrent density-voltage ($J-V$) curves of the NPFS-PSC devices with three different FTO etching depths (100, 150, and 200 nm) and the planar-PSC (without FTO etching); the reverse scanned results are also summarized in **Table 2**. As shown in Figure 4, the NPFS-based PSCs show a lower $J-V$ hysteresis behavior between forward scan and reverse scan than that for the planar-PSC. Additionally, the hysteresis behavior of NPFS-based PSCs was gradually decreased when the etching depth of FTO was increased from 100 to 200 nm. The improvement in hysteresis behavior of NPFS-based PSCs can be ascribed to the increasing of contact interfaces (FTO/TiO₂ and TiO₂/perovskite), which will influence the electron collection efficiency and decrease the hysteresis in PSC. Figure 4 also indicates that the NPFS-PSC devices exhibit higher PCE than the planar-PSC, particularly for the NPFS-200-PSC, which had the highest PCE (17.85%) with a short-circuit current density (J_{sc}) of 23.81 mA cm⁻², an open-circuit voltage (V_{oc}) of 1.06 V, and a fill factor (FF) of 0.71. Compared to the planar-PSCs, the J_{sc} was enhanced by 23.56% and the PCE improved by 25.61%. Interestingly, the improvement in PV performance of the NPFS-based PSC device was proportional to the etching depth of the FTO film, especially for the J_{sc} . As summarized in **Table 2**, deeper FTO etching-depths generated higher photocurrents from the NPFS-based PSCs. The various J_{sc} enhancement levels of the NPFS-based PSC devices likely results from two contributing factors, one optical and one electrical. In terms of the former, the light harvesting efficiency is enhanced due to the patterned FTO suppressing the Fresnel reflection loss at the glass/FTO interface by diffracting the incident light.^[23,24,40] The deeper etching depth improves the PCE by increasing the diffraction efficiency, which enables more photons to be captured from the incident light and more photocurrent to be generated from these captured photons. The latter contribution to increased photocurrent concerns improvement in carrier recombination (electrical property). The greater interfacial area and subsequently increased contact between the TiO₂-ml and the perovskite layer were proportional to the etched depth of the FTO. In addition, the patterned FTO also provided a larger interface of the FTO/TiO₂-cl than the planar

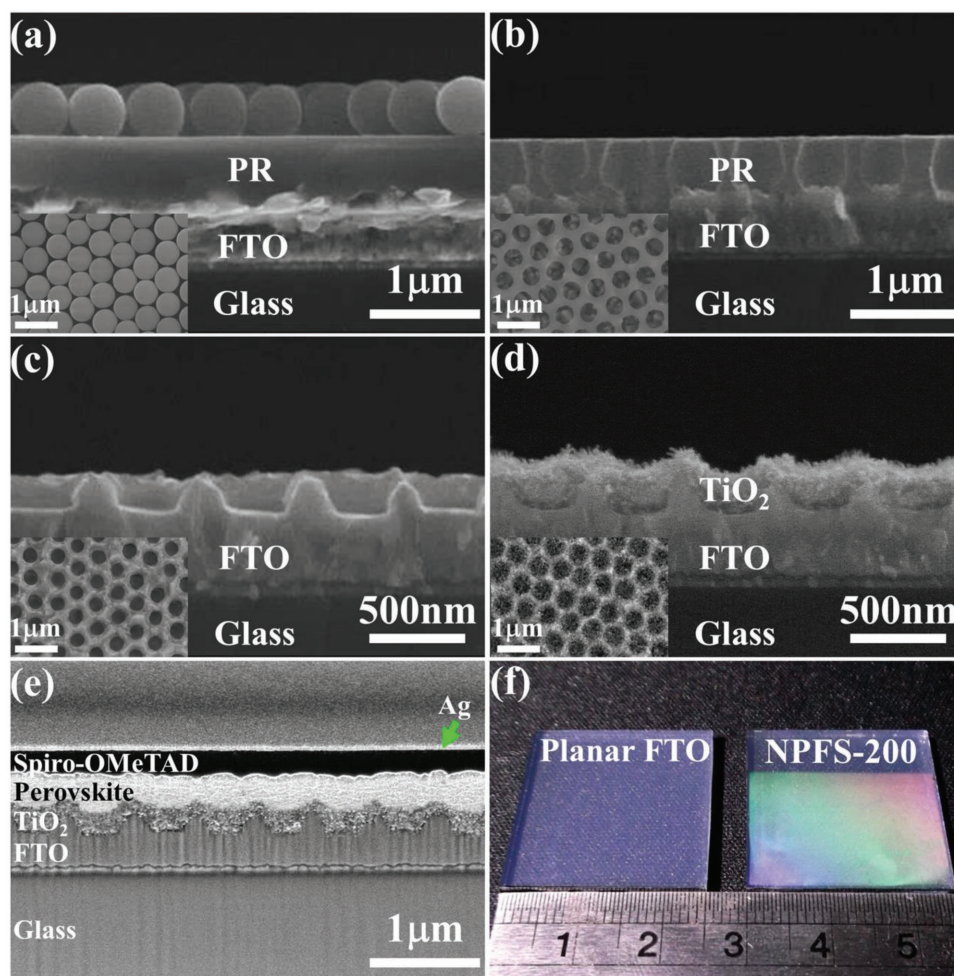


Figure 3. SEM imaging of a) monolayer spheres arrayed on glass substrates with a diameter of 500 nm. Inset: cross-sectional view, b) patterned photoresist structure. Inset: cross-sectional view, c) NPFS-200. Inset: cross-sectional view, d) NPFS-200 with $\text{TiO}_2\text{-cl}$ and $\text{TiO}_2\text{-ml}$. Inset: cross-sectional view, and e) NPFS-PSC with a structural period of 500 nm and an etching depth of 200 nm. f) Pictures of a planar FTO substrate and the NPFS-200 sample.

FTO, which directly influences the electron collection efficiency.^[28,33] The deeper FTO etching depth also translates into more interfacial contact at the FTO/ $\text{TiO}_2\text{-cl}$ interface, which considerably has the benefit of electron collection efficiency.

2.1. Optical Analysis of NPFS-Based Samples

To gain more insight into the influence of NPFS on the optical properties of a PSC, the reflectance spectra of different samples were measured using an integrating-sphere system with a wavelength range of 350 to 800 nm. The light source was normal incident from the glass side of the measured sample with the structure layout of glass/FTO/ $\text{TiO}_2\text{-cl}$ / $\text{TiO}_2\text{-ml}$ /MAPbI₃. **Figure 5a** shows the measured reflectance spectra of a planar-P, NPFS-100-P, NPFS-150-P, and NPFS-200-P, where the index P indicates the final layer was perovskite film. The NPFS-based samples presented lower reflectance spectra than the planar-P sample, especially for the NPFS-200-P, which showed the lowest reflectance spectrum over the entire

wavelength range (Figure 5a). The average reflectance of the planar-P, NPFS-100-P, NPFS-150-P, and NPFS-200-P was $\approx 6.59\%$, 5.77% , 5.55% , and 5.39% , respectively. Lower reflectance values indicate that more incident photons were absorbed by the perovskite layer due to the diffraction effect at the glass/FTO interface. Compared to the planar-P sample, the improvement in the average reflectance for the NPFS-200-P sample was about 22.16%.

To observe the behavior of incident photons within NPFS-based PSC devices, optical simulations were calculated using 3D finite-difference-time-domain (3D-FDTD) method. The simulation model was set up to evaluate the power absorption per unit volume and observe the absorption profile inside the perovskite layer for the different structures. Four different types of models were individually simulated: planar-P, an NPFS-100-P, an NPFS-150-P, and an NPFS-200-P. **Figure 5b** shows the simulated absorptivity spectra of perovskite layer with and without the NPFS structure. Compared to the planar-P (without NPFS), the NPFS-based simulations revealed higher absorption of incident photons from 500 to 800 nm. Moreover, the

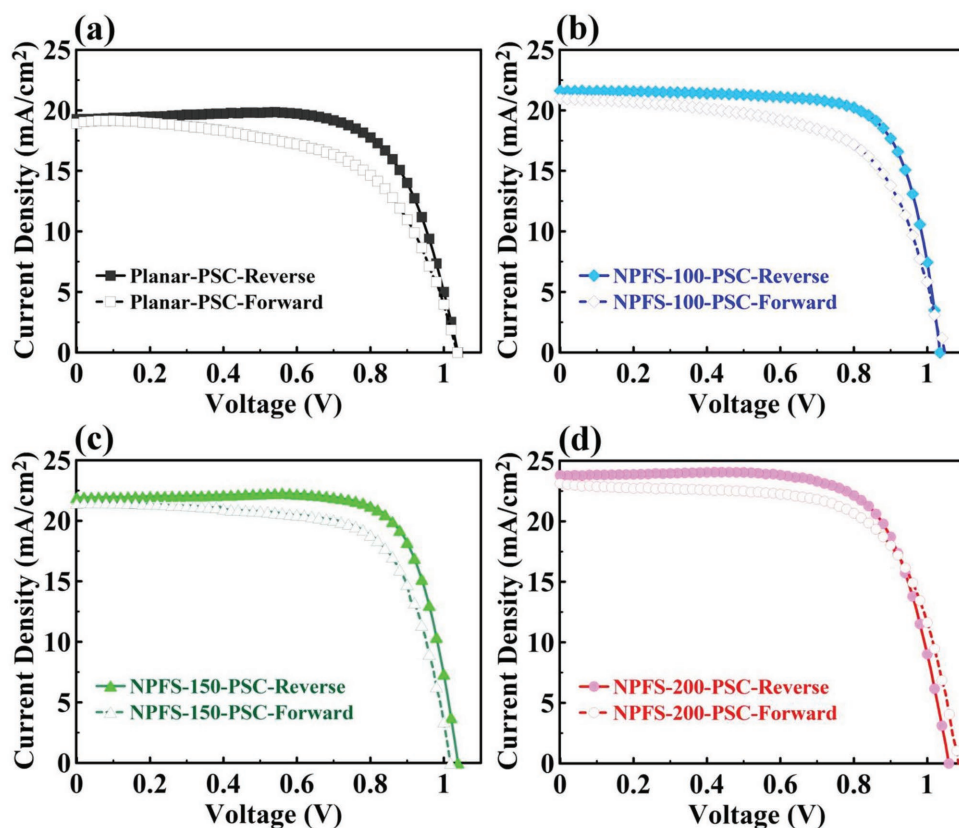


Figure 4. Forward scanned (solid line, filled symbols) and reverse scanned (dashed line, open symbols) photocurrent density–voltage (J – V) curves. a) Planar-PSC (without etching), b) NPFS-100-PSC (etching depth: 100 nm), c) NPFS-150-PSC (etching depth: 150 nm), and d) NPFS-200-PSC (etching depth: 200 nm).

improvement in the absorption of the NPFS-based simulations was also proportional to the etching depth of FTO. Greater structural depth facilitates absorbing more incident photons, consistent with the measurements reported in Figure 5a. Furthermore, Figure 5b indicates that the NPFS-200-P showed more effective light absorption at 470 to 800 nm than the planar-P and presented the highest increment of the absorptivity (about 10%) at 580 nm. To further investigate these experimental results, the absorption profiles inside of the perovskite layer of the different designed structures were also calculated (from the same individual simulation). Figure 5c provides the spatial profiles (with respect to the x – z plane) of the optical power absorption per unit volume at a wavelength of 550 nm for the planar-P, NPSF-100-P, NPFS-150-P, and NPFS-200-P. For ease of comparison, the color bar was set in the same scale range for the simulation results. As shown in Figure 5c, the

Table 2. Photovoltaic characteristics of NPFS-based PSC devices and the planar-PSC.

Device type	J_{sc} [mA cm ⁻²]	V_{oc} [V]	FF	PCE [%]
Planar-PSC	19.27	1.04	0.71	14.21
NPFS-100-PSC	21.63	1.04	0.74	16.48
NPFS-150-PSC	21.92	1.04	0.76	17.23
NPFS-200-PSC	23.81	1.06	0.71	17.85

NPFS-based simulations had stronger light absorption in the perovskite layer than the planar one. Furthermore, the light absorption density corresponded to the structural depth, the deeper structures gained more photons from the incident light due to the higher diffraction efficiency conferred by the NPFS (Figure 5c). In particular, the NPFS-200-P showed considerable improvement in light absorption compared to other NPFS-based samples. The absorption density of the planar-P had the highest value at the TiO₂-ml/perovskite boundary then gradually decayed in the perovskite layer. However, the absorption density of the NPFS-based case provided strong absorption at the TiO₂-ml/perovskite interface as well as in the central region of the perovskite layer. Consequently, the improvement in reflectance (Figure 5a) and light absorption (Figure 5b) over nearly the entire visible spectrum in the NPFS-based samples indicated that incorporating the patterned structure at the FTO/TiO₂ interface can to some extent increase the light absorbing ability of the perovskite absorber layer.

The simulation results in Figure 5 can be explained in diffractive grating by the following grating equation^[40,41]

$$k_0 \sin \theta_0 = k_g \sin \theta_g = k_p \sin \theta_m + mG = (2\pi / \lambda) n_{\text{eff}} \sin \theta_m + m(2\pi / \Lambda); m = \pm 1, \pm 2 \dots \quad (1)$$

$$\text{if } \theta_0 = 0 \rightarrow \sin \theta_m = m(\lambda / n_{\text{eff}} \Lambda); m = \pm 1, \pm 2 \dots \quad (2)$$

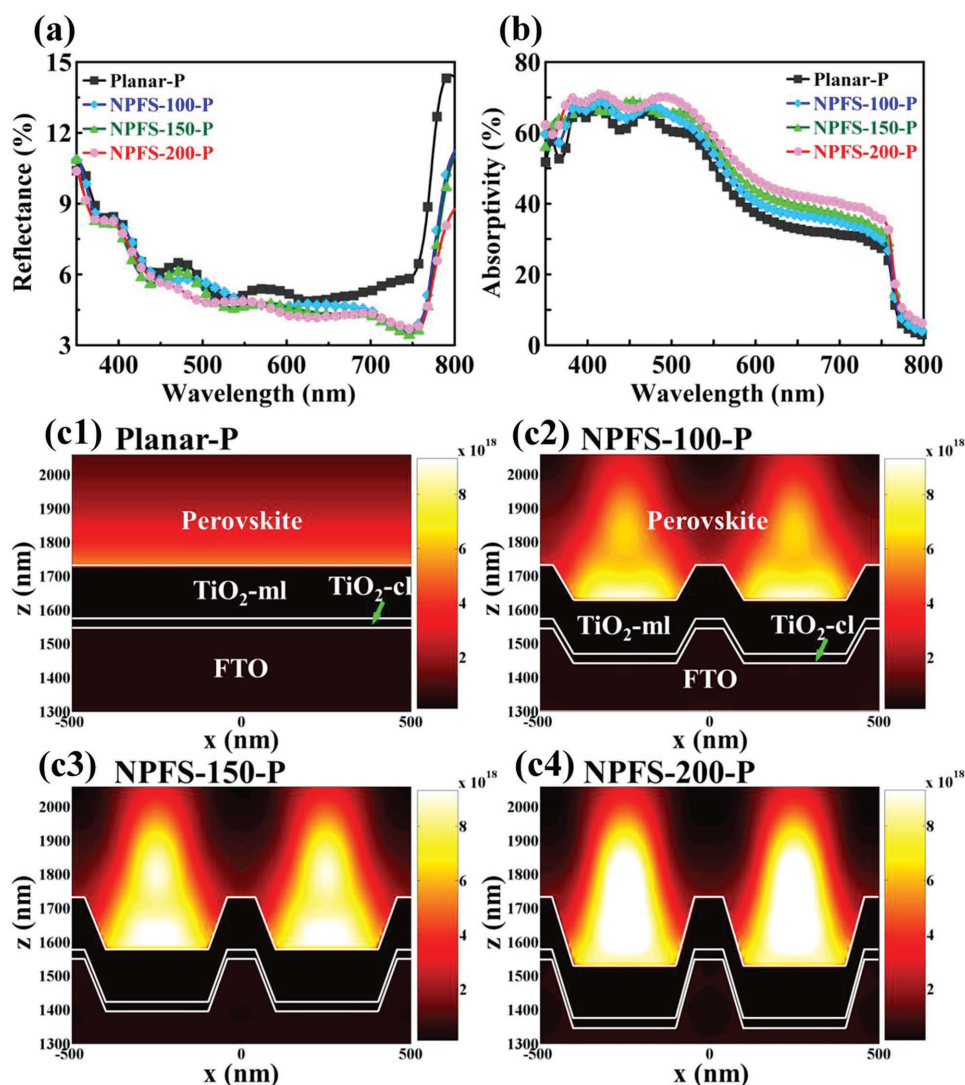


Figure 5. Optical analysis of a planar-P, NPFS-100-P, NPFS-150-P, and NPFS-200-P, respectively. a) Measurement of reflectance spectra. b) Simulation of absorptivity spectra. c) Simulated power absorption per unit volume distribution (observed wavelength: 550 nm).

where k_0 and θ_0 are the wavenumber and incident angle of the incident light, respectively, k_g and θ_g are the wavenumber and refraction angle of the light in the glass substrate, and k_p and θ_m indicate the wavenumber and diffraction angle of m th diffraction order for the diffracted light in the perovskite layer, G is the reciprocal grating constant of a periodic structure with a period of Λ , m is the m th diffraction order of the diffraction light, λ is the wavelength of the incident light in air, and n_{eff} is the effective refractive index of the FTO/perovskite layer. For a normal incident case ($\theta_0 = 0$), the diffraction grating equation (Equation (1)) can be reduced to Equation (2). As shown in Equation (2), the NPFS can make the normal incident light transfer some energy into the diffraction mode with a diffraction angle of θ_m . It has the benefit of absorbing more photons due to the increased optical path length of the perovskite layer. Additionally, the deeper structural depth induced a stronger diffraction effect (Figure 5). This can be explained by the diffraction efficiency, η_m ,

of Kirchhoff's diffraction theory (Equation (3)) for a phase grating using the following equation^[42]

$$\eta_m = \left(n_p \cos \theta_m / n_0 \cos \theta_0 \right)^2 t^2(\theta_0) \left[(1 - \cos 2m\pi f)(1 - \cos \Delta\phi) / m^2 \pi^2 \right]; m = \pm 1, \pm 2, \dots \quad (3)$$

where n_p and n_0 represent the refractive index of perovskite and air, respectively, $t(\theta_0)$ is the Fresnel transmission coefficient, f is the filling factor of grating, $\Delta\phi = (2\pi h/\lambda)(n_p \cos \theta_m - n_0 \cos \theta_0)$ is the phase difference of the rays passing through the grating region; and h is the groove depth of the grating. In the case of normal incident ($\theta_0 = 0$), deeper structural depths (h) will cause higher f and $\Delta\phi$ values, indicative of the higher diffraction efficiency of the m th diffraction mode. Therefore, the NPFS-200 allowed for stronger light absorption than the other cases.

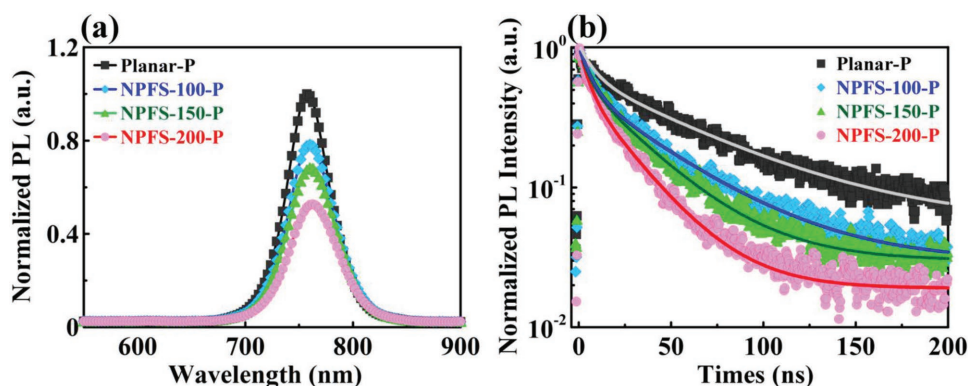


Figure 6. Measurement results of a) room temperature PL spectra and b) TRPL spectra for a planar-P, NPFS-100-P, NPFS-150-P, and NPFS-200-P with the glass/FTO/TiO₂-cl/TiO₂-ml/MAPbI₃ layout (without Ag anode).

2.2. Electrical Analysis of NPFS-Based Samples

Although the NPFS-based PSC was able to diffract the incident light and enhance light absorption efficiency, the average improvement in reflectance and absorptivity was still only about 22% and 6.7% (at 650 nm), respectively. These results are insufficient to explain the enhancement effect of the J_{sc} . Therefore, the electrical characteristics of the NPFS-based PSC also need to be taken into accounts. The TiO₂-ml is known to effectively extract the generated electrons from the perovskite layer in a TiO₂-based PSC. As mentioned above, the TiO₂-ml was deposited on a patterned FTO substrate instead of a planar one, which could directly influence the carrier collection and transfer efficiency of the TiO₂-based PSC. Herein, the steady-state photoluminescence (PL) and the time-resolved photoluminescence (TRPL) provided effective methods to analyze the electron extraction and transfer efficiency at the interface between the TiO₂-ml and perovskite film.^[43,44] **Figure 6a** shows the results of the room temperature PL spectra for a planar-P, an NPFS-100-P, an NPFS-150-P, and an NPFS-200-P with the layout of glass/FTO/TiO₂-cl/TiO₂-ml/MAPbI₃ (without Ag anode). As shown in **Figure 6a**, the peak value was at 760 nm, which represents the bandgap (1.63 eV) of a MAPbI₃-based PSC. Compared to the planar-P sample, the NPFS-based sample showed weaker emission intensity from the radiative recombination of carriers, which indicates that the NPFS-based PSC has higher electron extraction and transfer efficiency than the planar-PSC. **Figure 6b** shows the room temperature TRPL spectra of the different samples and the PL decay rate of each measurement was fitted by the global biexponential function $I(t) = A_1 \exp(-t/\tau_1) + A_2 \exp(-t/\tau_2)$, where A_1 and A_2 are the prefactors; τ_1 and τ_2 represent the lifetime of the fast and slow decay. The fitting parameters are summarized in **Table 3**.^[33,45,46] The fast decay may result from the carrier transfer from the perovskite layer to the electron contact area (cathode) and the slow decay could be attributed to the radiative recombination of the carriers before electron collection. As shown in **Table 3**, the fast and slow decay lifetimes of the NPFS-based samples were less than those of the planar-P sample, particularly for the NPFS-200-P. The fast decay lifetime was reduced from 7.12 to 5.09 ns with a ratio of 50.15% and the slow decay lifetime was increased from 51.78 to 25.15 ns with a ratio of 49.85%. This

suggests that the fast electron transfer and low carrier recombination of the NPFS-200-P leads to improved electron collection efficiency due to the increased interfacial contact area between FTO/TiO₂ and TiO₂/perovskite, then eventually contributes to the improved photogenerated current resulting in the enhancement of the PCE.

According to the analysis results discussed previously, the NPFS-200-based sample displayed enhanced performance in both the optical characteristics as well as in the electrical properties compared to other samples. Therefore, to further examine the enhancement of the device performance for the NPFS-200-based sample, the electro-chemical impedance spectroscopy (EIS) of a planar-PSC and NPFS-200-PSC were also measured. **Figure 7a** shows the Nyquist plots of the planar-P and the NPFS-200-P individually. The equivalent circuit in the inset of **Figure 7a** shows the three most important parameters: series resistance (R_s), carrier transfer resistance (R_{tr}), and recombination resistance (R_{rec}).^[47–49] Herein, the R_s can be obtained from the left intersection point to the Z'-axis of the left semicircle, which considers the resistance of all layers (including the electrode). Furthermore, the R_{tr} was associated with the contact resistance of the ETL/perovskite and perovskite/HTL interfaces, which relate to the left semicircle in the high-frequency range. In this investigation, the improvement of R_{tr} can only be attributed to the modification of the ETL/perovskite because the perovskite/HTL was identical in each case and the smaller semicircle correlated to the higher carrier transfer efficiency of a device. The R_{rec} was attributed to the interfacial recombination resistance of the ETL/perovskite, which is present in the low-frequency range as a transmission line (incomplete semicircle) and the higher R_{rec} indicates the lower recombination

Table 3. Parameters of TRPL spectra for PSC with and without NPFS.

Device type	τ_1 [ns]	Ratio_ τ_1 ^{a)} [%]	τ_2 [ns]	Ratio_ τ_2 ^{a)} [%]
Planar-P	7.12	19.67	51.78	80.33
NPFS-100-P	6.81	46.17	39.82	53.83
NPFS-150-P	6.59	46.11	33.06	53.89
NPFS-200-P	5.09	50.15	25.15	49.85

^{a)}The ratio_ $\tau_1 = A_1/(A_1 + A_2)$ and ratio_ $\tau_2 = A_2/(A_1 + A_2)$.

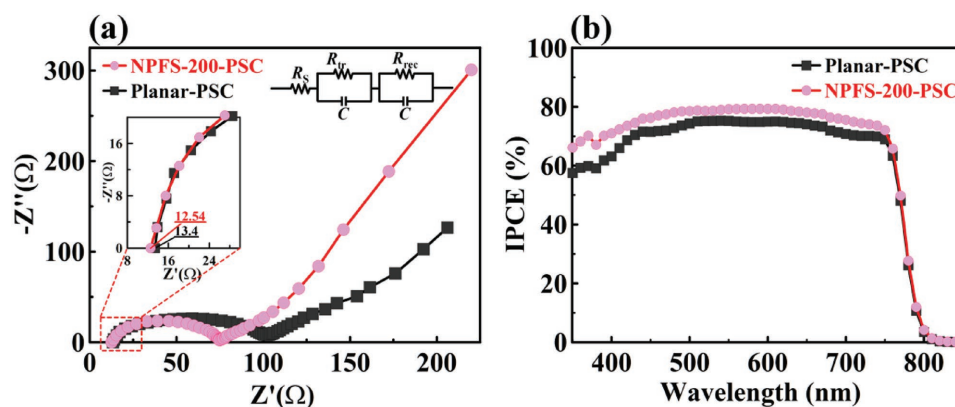


Figure 7. Measurement results of a) EIS spectra and b) IPCE spectra of the planar-PSC and NPFS-200-P, respectively.

rate of a device. As shown in the left inset of Figure 7a, the NPFS-200-P shows a slightly lower R_s value (12.54 Ω) than that of the planar-P (13.4 Ω) due to the increased interfacial contact area of the FTO/ETL. Additionally, the NPFS-200-PSC has a lower R_{tr} and higher R_{rec} than the planar-PSC (Figure 7a). This indicates that incorporating the NPFS in a PSC not improves carrier transfer efficiency but also suppresses the interfacial recombination due to the modified interface of the ETL/perovskite layer.

As discussed above, the NPFS-based PSC actualizes the potential of a high-PCE PSC device due to the benefits of both its optical and electrical properties, specifically for the NPFS-200-PSC. Therefore, the incident photon-to-current efficiency (IPCE) was used to further examine the performance of the planar-PSC and the NPFS-200-PSC (Figure 7b). The NPFS-200-PSC showed higher IPCE over the entire wavelength range. Referring to Figure 5b, the enhancement of the light absorption for the NPFS-200-P was mainly in the longer wavelength range (450 to 800 nm). Therefore, the increasing of the IPCE in the short wavelength range (350 to 450 nm) can be ascribed to the improvement of the electrical properties (Figures 6 and 7a). In spite of the NPFS-200-PSC shows the higher IPCE than the Planar-PSC over the entire wavelength range, the enhanced integrated photocurrent from IPCE was about 6% which was inconsistent with the improvement in measured J_{sc} of the same device (about 23%) listed in Table 2. The difference can be ascribed to the weak light source from monochromator as measuring the IPCE spectra, and the presence of trap-assistant recombination at interface of TiO_2 /perovskite. The weak light source will generate the less electrons than the strong light source. The interfacial defect at TiO_2 /perovskite will fill by holes and able to trap the electrons (recombination center).^[50,51] As illuminating with a weak monochromatic light on a PSC, generated electrons need to fill the recombination centers before electrons can be collected by electrode. By contrast, illuminating with a strong light source (100 mW cm^{-2}) on a PSC will generate more electrons from perovskite layer but only need to fill the same quantity of recombination centers. Therefore, the improvement phenomenon in J_{sc} due to enlarge interfaces of FTO/ TiO_2 and TiO_2 /perovskite was not obviously in IPCE spectra. Consequently, the NPFS-based PSCs have the ability to enhance light absorption in the perovskite layer (thus

generating more photocurrent) as well as to improve the charge transfer efficiency and decrease carrier recombination efficiency (thus collecting more electrons), which together result in a greatly increased PCE.

3. Conclusions

In summary, we have successfully developed a simple and rapid method to fabricate NPFS-PSC devices with different structural depths (100, 150, and 200 nm) by integrating the self-assembly method together with the sphere lithography technique. Through a series of optical measurement analyses, simulation evaluations, and electrical analyses of TRPL and EIS, NPFS-PSC devices have efficient light absorption due to reduced light reflection from the diffraction effect. Moreover, the NPFS-PSC also can improve the electron collection efficiency due to enhancing the carrier transfer efficiency and reducing the carrier recombination rate by increasing the interfacial contact area of the FTO/ETL and ETL/perovskite. Moreover, the improvement in both optical and electrical properties was proportional to the structural depth of the NPFS-based PSC. In comparison to the planar-PSC, the J_{sc} of NPFS-200-PSC was enhanced from 19.27 to 23.81 mA cm^{-2} leading to the PCE enhanced from 14.21% to 17.85%. Consequently, introducing the NPFS into the TiO_2 -based PSC represents a promising approach toward actualizing the potential of a high-performance PV device.

4. Experimental Section

Preparation of SiO_2 Nanospheres: Highly uniform SiO_2 nanospheres were prepared using the modified Stöber process in an alcohol-rich phase. Purified water, ammonium hydroxide, and fresh alcohol were added into a sealed bottle that was then purged with nitrogen and stirred to ensure full mixing; tetraethyl orthosilicate was then added into the system. After stirring for 2 h, the latex was centrifuged to collect the SiO_2 microspheres, which were then washed three times with fresh alcohol to remove any remaining impurities.^[36]

Fabrication of NPFS: The NPFS was fabrication by following procedures. First, the spin-coating method was used to deposit the commercially available positive photoresist film (S1805, Shipley Microposit) with a thickness of 600 nm onto an FTO glass substrate. Next, a monolayer of 500 nm diameter SiO_2 spheres was deposited onto

the photoresist layer to self-assemble. The samples were then exposed to a mask aligner (Q4000, Quintel Technology Ltd.) for 12 s and any residual spheres with an ultrasonic cleaner were removed for 10 min. According to standard procedure, a 0.15 M NaOH solution was used to develop the nanopatterned photoresist layer. Finally, this nanopatterned layer was transferred onto the FTO surface by ICP dry etching. The parameters for the ICP dry etching process were as follows: well-mixed BCl₃, Cl₂, and Ar gases, a reactor pressure of 7.5 mTorr, a top electrode RF power of 600 W, a bottom electrode RF power of 200 W, and a bias voltage of 210 V.

Fabrication of PSC: To produce the PSC, the FTO substrate was spin-coated with 30×10^{-3} M TiCl₄ (99%, Showa Chemical Industry Co., Ltd.) aqueous solutions at 2000 rpm for 60 s, followed by annealing at 180 °C for 5 min in air to form a TiO₂-cl with the film thickness of 30 nm. The spin-coating method was again used at 2000 rpm for 20 s to apply a 150 nm thick TiO₂-ml to serve as the ETL and followed by a thermal removal of the residual solvent at 120 °C for 5 min; the TiO₂-ml solution was prepared by dispersing commercial TiO₂ particles (P90, Evonik Industries) in ethanol with a concentration of 1.875 wt%. Next, the 320 nm thick absorber layer of MAPbI₃ was spin-coated and the excess at 100 °C was baked off for 1 h; the MAPbI₃ solution was prepared by dissolving the CH₃NH₃I and PbI₂ (molar ratio of CH₃NH₃I: PbI₂ was 1: 1) in a γ -butyrolactone (GBL)/dimethyl sulfoxide (DMSO) (volume ratio of GBL:DMSO was 1:1) solvent mixture. The Spiro-OMeTAD was then deposited by spin-coating method at 2000 rpm for 30 s to obtain a 220 nm thick HTL; the Spiro-OMeTAD that remained unbound after spin-coating was removed by oxidation for 30 min at room temperature in an open-air environment; the spiro-MeOTAD solution was prepared by dissolving 80 mg spiro-MeOTAD powders, 28 μ L of 4-tertbutylpyridine and 18 μ L of a stock solution of 520 mg mL⁻¹ lithium bis(trifluoromethylsulfonyl)imide in acetonitrile in 1 mL of chlorobenzene. Lastly, thermal evaporation was used to deposit a 100 nm thick Ag anode film to finish the PSC. The absorber layer and the HTL (excluding the oxidation process) were both fabricated in a glove box filled with nitrogen gas under 40% humidity. A single FTO substrate can be incorporated into nine individual devices in a single PSC fabrication procedure with a 2 mm \times 2 mm active area for each device. Consequently, the whole device is consisting of FTO/TiO₂-cl/TiO₂-ml/MAPbI₃/Spiro-OMeTAD/Ag either for the planar-PSC or for the NPFS-PSC.

FDTD Simulation: The FDTD simulation was conducted on FDTD-based software (FDTD Solutions, Lumerical Inc.). The simulation itself involved illuminating a plane-wave into a structure at normal incidence, generating two separated simulations (transverse electric and transverse magnetic mode light sources), and averaging the results incoherently. The absorption spectrum of the MAPbI₃-based solar cell ranges from 350 to 800 nm; therefore, these were chosen for the calculated wavelengths. The computational boundary of each simulation in the x -, y -, and z -direction was 1 μ m, 500 $\sqrt{3}$ nm, and 2.25 μ m, respectively. The calculated period of each simulation model in the x - and y -direction was 500 nm, which related to the diameter of the deposited SiO₂ spheres. In the z -direction, it was comprised of a 100 nm thick air layer, a 1 μ m thick glass substrate, a 550 nm thick FTO layer, a 30 nm thick TiO₂-cl, a 150 nm thick TiO₂-ml, and a 320 nm thick perovskite absorber layer. The simulation boundary in the x - and y -direction was set as the periodic boundary. In the z -direction, the upper and the lower boundary were surrounded by the perfectly matched layers with a reflectance lower than 10⁻⁸.

Device Characterization: The field-emission scanning electron microscopy (HITACHI S-4300, Hitachi Ltd.) was employed to observe the nanostructure properties of different samples. The sheet resistance was measured using the four-point probe method with a sourcemeter (Keithley 2400, Keithley Instruments Inc.). The photocurrent density–voltage (J – V) curves of the PSC devices were measured using a Keithley 2400 SourceMeter under AM 1.5G (global air mass of 1.5) illumination (YSS-50A, YAMASHITA) at a power density of one sun (100 mW cm⁻²); the scan rate was 0.2 V s⁻¹ with a voltage step of 0.01 V. The reflectance spectra of different samples were measured using an integrating-sphere

system that consisted of a UV–vis spectrometer (i-trometer, B&W Tek Inc.) and an integrating-sphere (MFS-630-005, Hong-Ming Technology Co., Ltd.). The PL spectra were measured using a photomultiplier tube detector system (PDS-1, DongWoo Optron Co., Ltd.), a monochromator (WELLS-001 FX, DongWoo Optron Co., Ltd.) as the photon-counting electronics, and a 440 nm continuous-wave diode laser (PDLH-440-25, DongWoo Optron Co., Ltd.) as the excitation light source. For the TRPL spectra, the excitation light source was a 440 nm pulse laser with an operating frequency of 312.5 MHz and a duration time of 1.08 μ s. The TRPL spectra were analyzed by a time-correlated single photon counting spectrometer (WELLS-001 FX, DongWoo Optron Co., Ltd.). The EIS spectra was measured on an electrochemical workstation (ZENNIUM, ZAHNER-Elektrik GmbH & Co. KG) with a 0.6 V bias and a frequency ranging from 1 MHz to 0.1 Hz under AM 1.5 G illumination conditions. The IPCE spectra of each sample were measured using a quantum efficiency measurement system (QER3011, Enli Technology Co., Ltd.) in DC mode.

Acknowledgements

The authors thank for the financial support of the Ministry of Science and Technology, Taiwan (Grant Nos. MOST 104-2221-E-008-092 and MOST 106-2218-E-182-005-MY2).

Conflict of Interest

The authors declare no conflict of interest.

Keywords

electron collection efficiency, light harvesting efficiency, nanopatterned substrates, perovskite, self-assembly, sphere lithography

Received: July 19, 2018
Revised: August 31, 2018
Published online:

- [1] A. Kojima, K. Teshima, Y. Shirai, T. Miyasaka, *J. Am. Chem. Soc.* **2009**, *131*, 6050.
- [2] W. S. Yang, J. H. Noh, N. J. Jeon, Y. C. Kim, S. Ryu, J. Seo, S. I. Seok, *Science* **2015**, *348*, 1234.
- [3] S. S. Shin, E. J. Yeom, W. S. Yang, S. Hur, M. G. Kim, J. Im, J. Seo, J. H. Noh, S. I. Seok, *Science* **2017**, *356*, 167.
- [4] W. S. Yang, B. W. Park, E. H. Jung, N. J. Jeon, Y. C. Kim, D. U. Lee, S. S. Shin, J. Seo, E. K. Kim, J. H. Noh, S. I. Seok, *Science* **2017**, *356*, 1376.
- [5] Y. Zhou, M. Yang, W. Wu, A. L. Vasiliev, K. Zhu, N. P. Padture, *J. Mater. Chem. A* **2015**, *3*, 8178.
- [6] J. H. Im, H. S. Kim, N. G. Park, *APL Mater.* **2014**, *2*, 081510.
- [7] H. Sun, K. Deng, Y. Zhu, M. Liao, J. Xiong, Y. Li, L. Li, *Adv. Mater.* **2018**, *30*, 1801935.
- [8] H. S. Ko, J. W. Lee, N. G. Park, *J. Mater. Chem. A* **2015**, *3*, 8808.
- [9] W. Nie, H. Tsai, R. Asadpour, J. C. Blancon, A. J. Neukirch, G. Gupta, J. J. Crochet, M. Chhowalla, S. Tretiak, M. A. Alam, H. L. Wang, A. D. Mohite, *Science* **2015**, *347*, 522.
- [10] E. J. Juárez-Pérez, M. Wußler, F. Fabregat-Santiago, K. Lakus-Wollny, E. Mankel, T. Mayer, W. Jaegermann, I. Mora-Sero, *J. Phys. Chem. Lett.* **2014**, *5*, 680.
- [11] D. W. deQuilletes, S. M. Vorpahl, S. D. Stranks, H. Nagaoka, G. E. Eperon, M. E. Ziffer, H. J. Snaith, D. S. Ginger, *Science* **2015**, *348*, 683.

- [12] W. Li, J. Fan, J. Li, Y. Mai, L. Wang, *J. Am. Chem. Soc.* **2015**, *137*, 10399.
- [13] G. Yang, C. Wang, H. Lei, X. Zheng, P. Qin, L. Xiong, X. Zhao, Y. Yan, G. Fang, *J. Mater. Chem. A* **2017**, *5*, 1658.
- [14] K. G. Lim, S. Ahn, Y. H. Kim, Y. Qi, T. W. Lee, *Energy Environ. Sci.* **2016**, *9*, 932.
- [15] J. Peng, Y. Wu, W. Ye, D. A. Jacobs, H. Shen, X. Fu, Y. Wan, T. Duong, N. Wu, C. Barugkin, H. T. Nguyen, D. Zhong, J. Li, T. Lu, Y. Liu, M. N. Lockrey, K. J. Weber, K. R. Catchpole, T. P. White, *Energy Environ. Sci.* **2017**, *10*, 1792.
- [16] Y. Xing, C. Sun, H. L. Yip, G. C. Bazan, F. Huang, Y. Cao, *Nano Energy* **2016**, *26*, 7.
- [17] N. Abdi, Y. Abdi, Z. Alemipour, *Solar Energy* **2017**, *153*, 379.
- [18] A. J. Pearson, G. E. Eperon, P. E. Hopkinson, S. N. Habisreutinger, J. T. W. Wang, H. J. Snaith, N. C. Greenham, *Adv. Energy Mater.* **2016**, *6*, 1600014.
- [19] Y. Z. Zheng, E. F. Zhao, F. L. Meng, X. SenLai, X. M. Dong, J. J. Wu, X. Tao, *J. Mater. Chem. A* **2017**, *5*, 12416.
- [20] J. Song, E. Zheng, X. F. Wang, W. Tian, T. Miyasaka, *Sol. Energy Mater. Solar Cells* **2016**, *144*, 623.
- [21] E. Nouri, M. R. Mohammadi, P. Lianos, *Carbon* **2018**, *126*, 208.
- [22] J. Yoon, H. Sung, G. Lee, W. Cho, N. Ahn, H. S. Jung, M. Choi, *Energy Environ. Sci.* **2017**, *10*, 337.
- [23] S. M. Kang, S. Jang, J. K. Lee, J. Yoon, D. E. Yoo, J. W. Lee, M. Choi, N. G. Park, *Small* **2016**, *12*, 2443.
- [24] M. T. Hö rantner, W. Zhang, M. Saliba, K. Wojciechowski, H. J. Snaith, *Energy Environ. Sci.* **2015**, *8*, 2041.
- [25] M. M. Tavakoli, K. H. Tsui, Q. Zhang, J. He, Y. Yao, D. Li, Z. Fan, *ACS Nano* **2015**, *9*, 10287.
- [26] K. Yamamoto, T. Kuwabara, K. Takahashi, T. Taima, *Jpn. J. Appl. Phys.* **2015**, *54*, 08KF02.
- [27] J. Wei, R. P. Xu, Y. Q. Li, C. Li, J. D. Chen, X. D. Zhao, Z. Z. Xie, C. S. Lee, W. J. Zhang, J. X. Tang, *Adv. Energy Mater.* **2017**, *7*, 1700492.
- [28] D. L. Wang, H. J. Cui, G. J. Hou, Z. G. Zhu, Q. B. Yan, G. Su, *Sci. Rep.* **2016**, *6*, 18922.
- [29] T. Salim, S. Sun, Y. Abe, A. Krishna, A. C. Grimsdale, Y. M. Lam, *J. Mater. Chem. A* **2015**, *3*, 8943.
- [30] N. J. Jeon, J. H. Noh, Y. C. Kim, W. S. Yang, S. Ryu, S. I. Seok, *Nat. Mater.* **2014**, *13*, 897.
- [31] D. Liu, M. K. Gangishetty, T. L. Kelly, *J. Mater. Chem. A* **2014**, *2*, 19873.
- [32] C. Momblona, O. Malinkiewicz, C. Roldán-Carmona, A. Soriano, L. Gil-Escrig, E. Bandiello, M. Scheepers, E. Edri, H. J. Bolink, *APL Mater.* **2014**, *2*, 081504.
- [33] X. Zheng, Z. Wei, H. Chen, Q. Zhang, H. He, S. Xiao, Z. Fan, K. S. Wong, S. Yang, *Nanoscale* **2016**, *8*, 6393.
- [34] S. S. Mali, C. A. Betty, P. S. Patil, C. K. Hong, *J. Mater. Chem. A* **2017**, *5*, 12340.
- [35] J. Choi, S. Song, M. T. Hö rantner, H. J. Snaith, T. Park, *ACS Nano* **2016**, *10*, 6029.
- [36] C. H. Hou, S. Z. Tseng, C. H. Chan, T. J. Chen, H. T. Chien, F. L. Hsiao, H. K. Chiu, C. C. Lee, Y. L. Tsai, C. C. Chen, *Appl. Phys. Lett.* **2009**, *95*, 133105.
- [37] M. C. Liu, C. R. Lin, C. H. Chan, *AIP Adv.* **2016**, *6*, 115013.
- [38] S. Z. Tseng, C. R. Lin, H. S. Wei, C. H. Chan, S. H. Chen, *Int. J. Photoenergy* **2014**, *2014*, 707543.
- [39] C. R. Lin, M. C. Liu, Y. C. Chiu, C. H. Chan, *Appl. Phys. Lett.* **2017**, *110*, 093101.
- [40] Y. Wang, P. Wang, X. Zhou, C. Li, H. Li, X. Hu, F. Li, X. Liu, M. Li, Y. Song, *Adv. Energy Mater.* **2018**, *8*, 1702960.
- [41] Y. H. Ho, K. Y. Chen, K. Y. Peng, M. C. Tsai, W. C. Tian, P. K. Wei, *Opt. Express* **2013**, *21*, 8535.
- [42] X. Jing, Y. Jin, *Appl. Opt.* **2011**, *50*, C11.
- [43] Y. Li, L. Meng, Y. Yang, G. Xu, Z. Hong, Q. Chen, J. You, G. Li, Y. Yang, Y. Li, *Nat. Commun.* **2016**, *7*, 10214.
- [44] F. Zhou, H. Liu, X. Wang, W. Shen, *Adv. Funct. Mater.* **2017**, *27*, 1606156.
- [45] Y. Yang, K. Ri, A. Mei, L. Liu, M. Hu, T. Liu, X. Li, H. Han, *J. Mater. Chem. A* **2015**, *3*, 9103.
- [46] H. Zhang, J. Cheng, F. Lin, H. He, J. Mao, K. S. Wong, A. K. Y. Jen, W. C. H. Choy, *ACS Nano* **2016**, *10*, 1503.
- [47] Y. Wang, W. Y. Rho, H. Y. Yang, T. Mahmoudi, S. Seo, D. H. Lee, Y. B. Hahn, *Nano Energy* **2016**, *27*, 535.
- [48] K. Wang, C. Liu, P. Du, J. Zheng, X. Gong, *Energy Environ. Sci.* **2015**, *8*, 1245.
- [49] D. Yang, R. Yang, J. Zhang, Z. Yang, S. Liu, C. Li, *Energy Environ. Sci.* **2015**, *8*, 3208.
- [50] T. S. Sherkar, C. Momblona, L. Gil-Escrig, J. Ávila, M. Sessolo, H. J. Bolink, L. J. A. Koster, *ACS Energy Lett.* **2017**, *2*, 1214.
- [51] J. Haruyama, K. Sodeyama, I. Hamada, L. Han, Y. Tateyama, *J. Phys. Chem. Lett.* **2017**, *8*, 5840.